Acta Materialia 251 (2023) 118903

Contents lists available at ScienceDirect

Acta Materialia

journal homepage: www.elsevier.com/locate/actamat

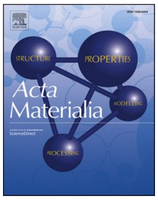

Identifying the effect of coherent precipitates on the deformation mechanisms by in situ neutron diffraction in an extruded magnesium alloy under low-cycle fatigue conditions

D. Xie [a,#], Z.H. Li [b,#], T.T. Sasaki [b,*], Y.F. Gao [a,*], Z.Y. Lyu [a], R. Feng [c], Y. Chen [c], K. An [c], H.B. Chew [d], T. Nakata [e], S. Kamado [e], K. Hono [b], P.K. Liaw [a]

[a] *Department of Materials Science and Engineering, The University of Tennessee, Knoxville, TN 37996, USA*
[b] *National Institute for Materials Science, 1-2-1 Sengen, Tsukuba, 305-0047, Japan*
[c] *Neutron Scattering Division, Oak Ridge National Laboratory, Oak Ridge, TN 37831, USA*
[d] *Department of Aerospace Engineering, University of Illinois at Urbana-Champaign, Urbana IL 61801, USA*
[e] *Nagaoka University of Technology, 1603-1, Kamitomioka, Nagaoka, 940-2188, Japan*

ARTICLE INFO

Keywords:
Low cyclic fatigue
Magnesium alloy
In situ neutron diffraction
G.P. zones

ABSTRACT

As a new class of heat-treatable magnesium alloys, the low-alloyed Mg-Al-Ca-Mn alloy has great engineering potential because of its excellent extrudability and high strength by the dispersion of Guinier-Preston (G.P.) zones. The complex deformation mechanisms associated with hexagonal crystals, the interactions between defects with such G.P. zones, as well as their impacts on fatigue lifetime, are all critical issues before the actual deployment of such materials. In this study, this type of Mg alloy with and without G.P. zone dispersion during cyclic deformation was investigated by *in situ* neutron diffraction measurements. The relationship between the macroscopic cyclic deformation behavior and the microscopic response (particularly twinning and detwinning) at the grain level was established. The general deformation mechanism evolution in samples under the solution-treated (S.T.) state was generally similar to that in samples under the peak-aged (P.A.) state. Both samples plastically deformed by extension twinning during compression, and by a sequential process of detwinning and dislocation motion under reverse tension. Results suggest that the precipitates provided the greatest strengthening against the prismatic slip (~ 45% increase), the moderate to the $\{10\bar{1}2\}$ extension twinning (~ 27 %), and the least to the basal slip (~ 11% increase). The P.A. samples have shorter fatigue lifetime primarily due to the excessive dislocation pileups and the higher backstress that promote crack initiation.

1. Introduction

Magnesium (Mg) alloys are potential structural materials driven by excellent properties such as low density (2/3 that of aluminum and 1/4 that of iron), high strength-to-weight ratio, high specific stiffness, and superior fatigue resistance [1–3]. Detailed knowledge of the fatigue behavior and lifetime prediction of Mg alloys as structural materials is vital for the use and evaluation of the mechanical reliability of these materials as structural components.

The intrinsic nature of the hexagonal-close-packed (HCP) crystal structure has limited the wide application of Mg alloys, due to the poor strength-ductility combination resulting from the limited number of plastic deformation modes. Significant work has been conducted to improve the mechanical properties of Mg alloys. An increasing interest in Mg alloys is to develop new alloy systems with novel precipitates because the precipitation strengthening can lead to additional strength

---

[*] Corresponding authors.
E-mail addresses: SASAKI.Taisuke@nims.go.jp (T.T. Sasaki), ygao7@utk.edu (Y.F. Gao).

[#] These two authors contribute equally to this paper.

https://doi.org/10.1016/j.actamat.2023.118903
Received 14 November 2022; Received in revised form 26 February 2023; Accepted 2 April 2023
Available online 3 April 2023

at wide temperatures range [4–6], achieve excellent extrudability and high strength simultaneously in extrusions [7,8], overcome formability-strength trade-off in sheets [9–11], and be leveraged with additions of rare-earth (RE) elements [12–14]. The investigation concerning the strengthening effect of precipitates on the major slip and twinning modes becomes essential. Nie [15] developed the Orowan equation appropriate for magnesium alloys strengthened by the different types of precipitates. The basal plate-shaped precipitates are ineffective in impeding the basal slip, but they have an excellent strengthening effect against the prismatic slip and twinning [16]. The prismatic/pyramidal plate-like precipitates have a strong blocking effect on the basal slip [15], but are weak in impeding prismatic slip and twinning-mediated plasticity [17]. Rod-like precipitates were also reported to obstruct prismatic slip and basal slip but had a negligible effect on twinning and pyramidal slip [18,19]. Despite these progresses, the above conclusions were derived for monotonic loading conditions and therefore might not be applicable under complex cyclic loading histories due to the nature of the anisotropic plasticity that also depends on texture and loading directions [20,21]. The backstress [19,22] caused by these precipitates during cyclic low-magnitude deformation may affect not only the formation of twinning but also the detwinning and residual twins [20,23,24]. It is thus necessary to understand the effect of precipitates on the cyclic deformation modes of Mg alloys. For example, the plastic deformation could be controlled by the alternative $\{10\bar{1}2\}$ extension twinning and detwinning under cyclic loading [20,21,23,25], but the contributions from precipitates during such alternating and evolving processes remain elusive.

In addition to the above complexities in the interactions of dislocation/twin and precipitates, the resulting damage initiation and accumulation processes are equally complicated. Of particular interest here is the lifetime in the low-cycle-fatigue (LCF) condition. It is well known that the material strength and LCF lifetime have a reverse correlation in face-centered-cubic and body-centered-cubic materials, in which the dominant failure mechanism is the accumulation of strains on the persistent slip bands (PSBs). For Mg alloys with or without the precipitates, PSBs interact with the complex twinning/detwinning processes. The activation sequence of various dislocation slip, twining, and detwinning systems, together with the presence of strengthening precipitates, may lead to a unique synergistic effect on the LCF lifetime.

The above challenges, namely, the deformation and damage mechanisms of Mg alloys under LCF conditions, are oftentimes investigated from transmission electron microscopy (TEM) and other advanced characterization tools. Nevertheless, these methods are post-mortem and destructive, so that a complete scenario and a quantitative determination of various contributing mechanisms cannot be obtained. These issues can be mitigated by the state-of-the-art neutron diffraction technique that provides both in situ (real time as well) and nondestructive measurements, from which the microstructural level knowledge of how grain families and twin systems interact. Neutron beams are highly penetrating so they can be used as a non-destructive probe in severe environments [26]. The wavelengths of neutrons are similar to atomic spacing, which makes them useful for determining the information, i.e., the evolution of crystal structures, intensity, and lattice strain during plastic deformation. In the present work, we utilize one of the leading neutron facilities in the world to investigate a novel Mg alloy that can be heat-treated to generate coherent precipitates [plate-like Guinier-Preston (G.P.) zones]. To our best knowledge, the effect of coherent precipitates on the fatigue behavior of Mg alloys has been rarely investigated at the grain level. Coupling with the *in situ* neutron diffraction, it is possible to obtain detailed microstructural information that leads to an in-depth understanding of the LCF behavior of advanced Mg alloys with and without the presence of coherent precipitates. Results from this work can therefore provide tremendous opportunities for future improvement in Mg alloy design.

2. Experimental details

2.1. Material

The Mg alloy used in this study was an extruded AXM10304 Mg alloy with the composition of Mg-1.3Al-0.3Ca-0.4Mn (weight percent, wt.%). After homogenization at 500 °C for 1 h, the sample was indirectly extruded at 250 °C at a die-exit speed of 22 m/min with an extrusion ratio of 7.5 without lubrication to obtain extruded bars of 15 mm in diameter. To investigate the effect of G.P. zone dispersion on the fatigue behavior of the Mg alloy, one sample was subjected to solution treatment at 500 °C for 30 min in an electronic furnace under an Ar atmosphere followed by water quenching (denoted as the S.T. sample throughout the present work). The other was subjected to artificial aging at 200 °C for 30 min in an oil bath after solution treatment (denoted as the P.A. sample throughout this paper). The dog-bone-shaped samples with gauge dimensions of ϕ8mm × 16 mm were cut with the longitudinal axes parallel to the extruded direction (ED) of the extruded bar for mechanical testing.

2.2. Real-time in situ neutron diffraction measurements

The *in situ* neutron diffraction measurement was performed at the VULCAN Engineering Materials Diffractometer [27–30], the Spallation Neutron Source (SNS), Oak Ridge National Laboratory (ORNL) during fully reversed low-cycle fatigue under a continuous-loading condition [24]. In this study, the sample was mounted horizontally to the VULCAN load frame, with the axial direction parallel to ED. The angle between the incoming neutron beam and the specimen was 45°. The two stationary detector banks are located at ± 90° to the incoming beam, simultaneously recording two complete diffraction patterns with diffraction vectors parallel (Q||) and perpendicular (Q⊥) to the applied load, respectively. The macroscopic strain was measured using an extensometer attached to the sample during *in situ* neutron diffraction measurement. The schematic neutron experimental setup is shown in Fig. 1. The neutron beam slits are 7 mm (horizontal) × 7 mm (vertical), using a 5 mm receiving collimator, leading to a neutron gauge total volume of 245 mm^3. The neutron diffraction measurements were conducted under the high-intensity mode with a chopper speed of 30 Hz with a center wavelength of 2.7 Å, which corresponds to a lattice d-spacing of 0.9~3.2 Å. After the measurement, the data was analyzed, employing VULCAN Data Reduction and Interactive Visualization software (VDRIVE) [31]. The neutron diffraction data were chopped into time bins with a time interval of 2 min. The lattice strains of a given orientation (hkil) plane to the detector banks can be calculated based on the peak shift between the loaded and load-free patterns, given by:

$$\varepsilon_{hkil} = \frac{d_{hkil} - d^0_{hki.l}}{d^0_{hkil}} \tag{1}$$

where d_{hkil} and d^0_{hkil} are the plane d-spacings under the strained and unstrained conditions, respectively. The counting time for the undeformed sample was 10 min to reduce the propagated d^0_{hkil} statistic error. It is worth noting that the d^0_{0002} in the axial direction is absent due to the strong initial fiber in the S.T. and P.A. samples. To obtain the d-spacing of the {0002} reflection for the load-free condition, we followed the approach developed by Brown et al. [32]. Due to the elastically isotropic nature of Mg alloys, the ratios between the (hkil) peak positions in banks 1 and 2 should be identical in load-free conditions. Therefore, in this paper, we use the d^0_{0002} in the radial direction as the initial d-spacings of {0002} reflection peak under the unstrained conditions in the axial direction in this paper.

The fully reversed strain-controlled low-cycle fatigue experiment was conducted with a total strain amplitude of ±1% at room temperature. The fatigue cycles, initial compression, 1st, 2nd, 5th, 10th, 20th, 30th, 50th, 80th, 110th, and 140th cycles were selected for the real-time *in situ*

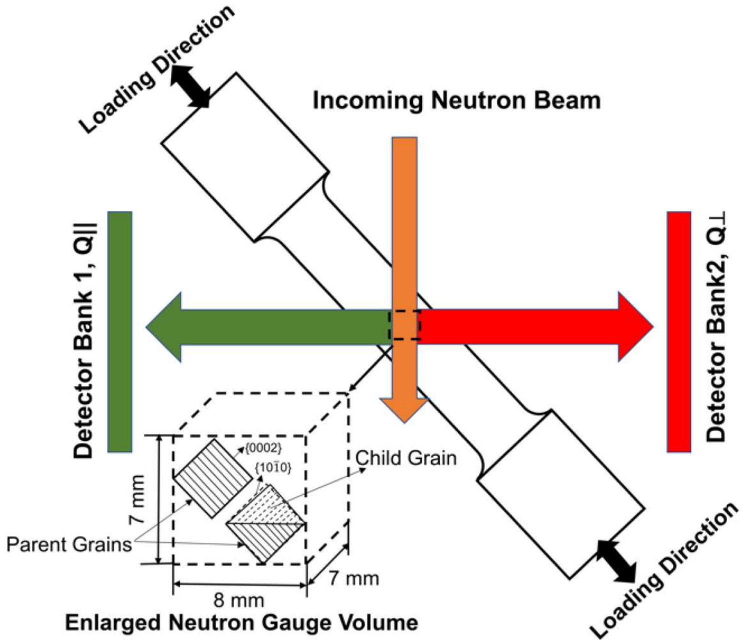

Fig. 1. A schematic setup at Vulcan, SNS, ORNL. The loading axis is parallel to the extrusion direction (ED) of samples.

neutron diffraction measurements for the S.T. sample, and 1st, 2nd, 5th, 10th, 20th, 30th, 50th, 70th, and 90th cycles for the P.A. sample. A strain rate of 7.4×10^{-6} s^{-1} was adopted for the initial compression, 1st, and 2nd cycles, and 1.11×10^{-5} s^{-1} for the other chosen cycles. For the other remaining cycles, a strain rate of 1.0×10^{-2} s^{-1} was applied.

2.3. Microstructure characterization

Electron backscatter diffraction (EBSD) analyses were performed at 20 kV using a field emission scanning electron microscope (SEM), Carl Zeiss Cross Beam 1540EsB, equipped with Oxford Instruments HKL EBSD detector and AZtec analysis software package. Samples for EBSD measurements were mechanically ground by silicon carbide (SiC) papers (#800, #2000, and #4000), followed by alumina (AP-D Powder, 0.05 μm) and silica suspension (OP-S NonDry, 0.25 μm) polishing. The polished samples were then cleaned using a Hitachi IM4000 ion milling system. Transmission electron microscopy (TEM) observations were carried out, using FEI Tecnai 20 and Titan G2 80–200 TEMs operated at 200 kV. Thin foil samples for TEM observations were mechanically ground to ~ 150 μm in thickness, using series SiC papers, and subsequently punched to discs of 3 mm in diameter. The discs were twin-jet electropolished in a solution of 5.3 g LiCl, 11.2 g $Mg(ClO_4)_2$, 500 ml methanol, and 100 ml 2-butoxy-ethanol at ~ 50 °C and ~ 0.1 A, and finally cleaned using Gatan 691 precision ion polishing system (Gatan PIPS) at 2 kV for 20 min.

3. Results

3.1. Macroscopic mechanical behavior

The mechanical stress-strain responses of the S.T. and the P.A. samples in the chosen fatigue cycles are displayed in Figs. 2(a) and (b), respectively. It is noticed that the shape of stress-strain hysteresis loops of the S.T. sample is similar to those of the P.A. sample since the 2nd cycle, which is asymmetric throughout the whole fatigue lifetime. The stress-strain hysteresis loop during reverse tension exhibited a more significant sigmoidal shape (or S-shape) in the P.A. sample and a less obvious one in the S.T. sample. The 0.2% proof stress during reverse

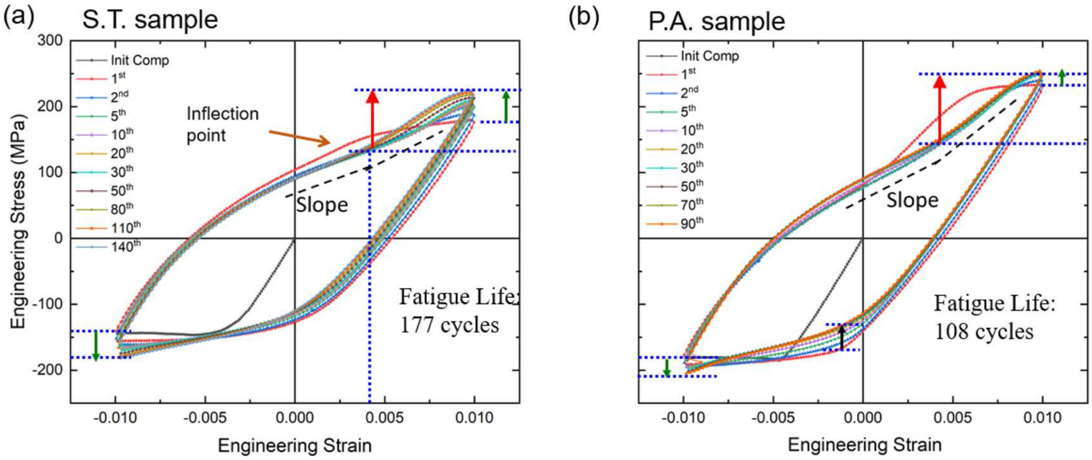

Fig. 2. The macroscopic mechanical stress-strain response in the S.T. sample (a) and P.A. sample (b). The red arrows indicate the strain hardening, green arrows suggest the cyclic hardening.

tension is significantly smaller than that during compression in both samples, which is attributed to the early occurrence of the detwinning process during revere tension. Meanwhile, the 0.2% proof stress during compression gradually decreased in the P.A. sample, indicated by the black arrow in Fig. 2(b), while almost keeping stable in the S.T. sample. The aging treatment results in an apparent increase in the tensile and compressive peak stresses. Although the AXM10304 Mg alloy specimens under the above two conditions exhibit similar ductility, based on the uniaxial tension test [7], the fatigue life of the P.A. sample was reduced to 108 cycles (~ 35% decrease), compared with 177 cycles in the S.T. sample. Furthermore, a relatively large strain hardening is observed in the P.A. sample (indicated by the red arrows), while the S.T. sample shows a relatively large cyclic hardening (indicated by the green arrows). The reasons that cause these differences will be elaborated in detail in the following sections.

3.2. *Microscopic response by neutron diffraction*

3.2.1. *Diffraction peak intensity evolution*

The diffraction peak intensity evolutions of certain hkils in the axial detector bank for the S.T. and P.A. samples from the real-time *in situ* neutron diffraction measurements are illustrated in Figs. 3(a) and (b), respectively. The detwinning and twinning modes are perceived as the {0002} diffraction peak intensity experiencing a decreasing-increasing sequence accompanied by an increasing-decreasing sequence in the $\{10\bar{1}0\}$ diffraction peak intensity in each selected fatigue cycle [33]. The value of the $I_{0002}^{-1\%}$ ({0002} peak intensity at a strain of -1%) keeps increasing until the 20th cycle and then ceases changing, suggesting that the twinning activities continued enhancing in the first 20 cycles in the S.T. sample. In contrast, the value of $I_{0002}^{-1\%}$ gradually increased in the P.A. sample, indicating that the twin fraction increased during compression with the fatigue cycles. Same as previous reports on the wrought Mg alloys [12,15,16], residual twins are gradually accumulated in the S.T. (since the 20th cycle) and P.A. sample (since the 50th cycle) under cyclic loading, indicated by the fact that the $I_{0002}^{1\%}$ ({0002} peak intensity at the strain of +1%) did not go back to 0 in these cycles.

The diffraction peak intensities of the {0002} grains in the axial detector bank as a function of engineering stress during tension and compression in each selected fatigue cycle for both S.T. and P.A. samples are demonstrated in Fig. 4. The slopes of {0002} intensity with applied stress can indicate that the deformation mode directly, as the intensity variation in the twin-related grains (i.e., {0002} and $\{10\bar{1}0\}$) is caused by the twinning/detwinning process [20,24]. The dashed lines in Fig. 4 represent the general trends of the diffraction intensity evolution with stress in certain fatigue cycles. The capitalized letters, "D", "DT", "T", "TR1", and "TR2", represent the dislocation-controlled mode, detwinning-controlled mode, twinning-controlled mode, and transition from twinning to dislocation-controlled mode during compression, and transition from detwinning to dislocation-controlled mode during reverse tension, respectively, which are used throughout the entire paper.

As shown in Fig. 4(a), upon tension, the S.T. sample first experiences no change, then a decrease that is related to the detwinning process "DT", another decrease with a relatively small slope that is corresponding to the transition from the detwinning to dislocation process "TR2", and eventually a plateau that is related to the dislocation process "D" over fatigue cycles. The activation of the dislocation motion in the "D" region is responsible for the rapid strain hardening in the macroscopic stress-strain curve, which is marked by the red arrow in Fig. 2. This region is characterized by a relatively steeper slope, as shown in Fig. 2, indicating a greater degree of strain hardening. However, it should be noted that the overall strain hardening effect is not significant due to the relatively small strain amplitude, which amounts to a total amplitude of only ±1% in this paper. A similar trend is observed in the P.A. sample during tension, as presented in Fig. 4(b). Upon compression, the intensity in the S.T. sample in Fig. 4(c) first remains unchanged, and then suddenly increases due to the twinning mode "T". Another increase but with a small slope is identified since the 5th cycle, which is related to the transition from the twinning to dislocation-dominated deformation region "TR1". As shown in Fig. 4(d) for the P.A. sample, upon compression, a similar sequence of deformation model evolution is observed, and the transition region is found since the 10th cycle. It is worth pointing out that although the dislocation slip in the transition region became more active, twinning is still the dominant deformation mode, which results in relatively small strain hardening in the "TR1" region.

3.2.2. *Lattice strain evolution*

In general, upon the initial compression, the lattice strain evolution of certain interested hkils in the S.T. sample resembled that in the P.A.

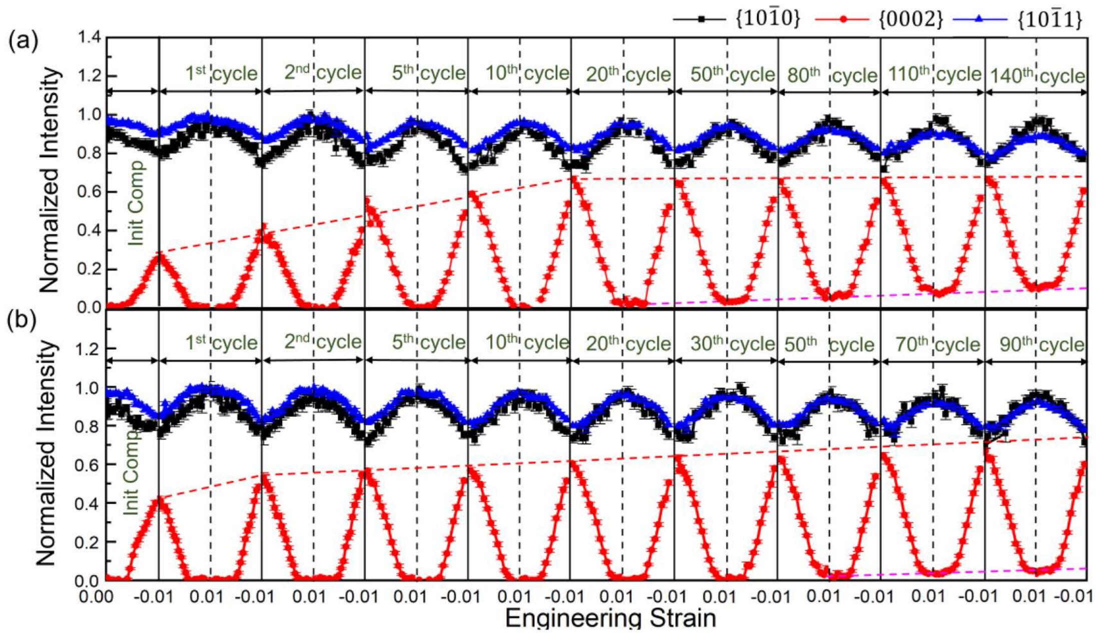

Fig. 3. The diffraction peak intensity evolution of certain hkils in selected fatigue cycles in the axial detector bank for the S.T. sample (a), and P.A. sample (b).

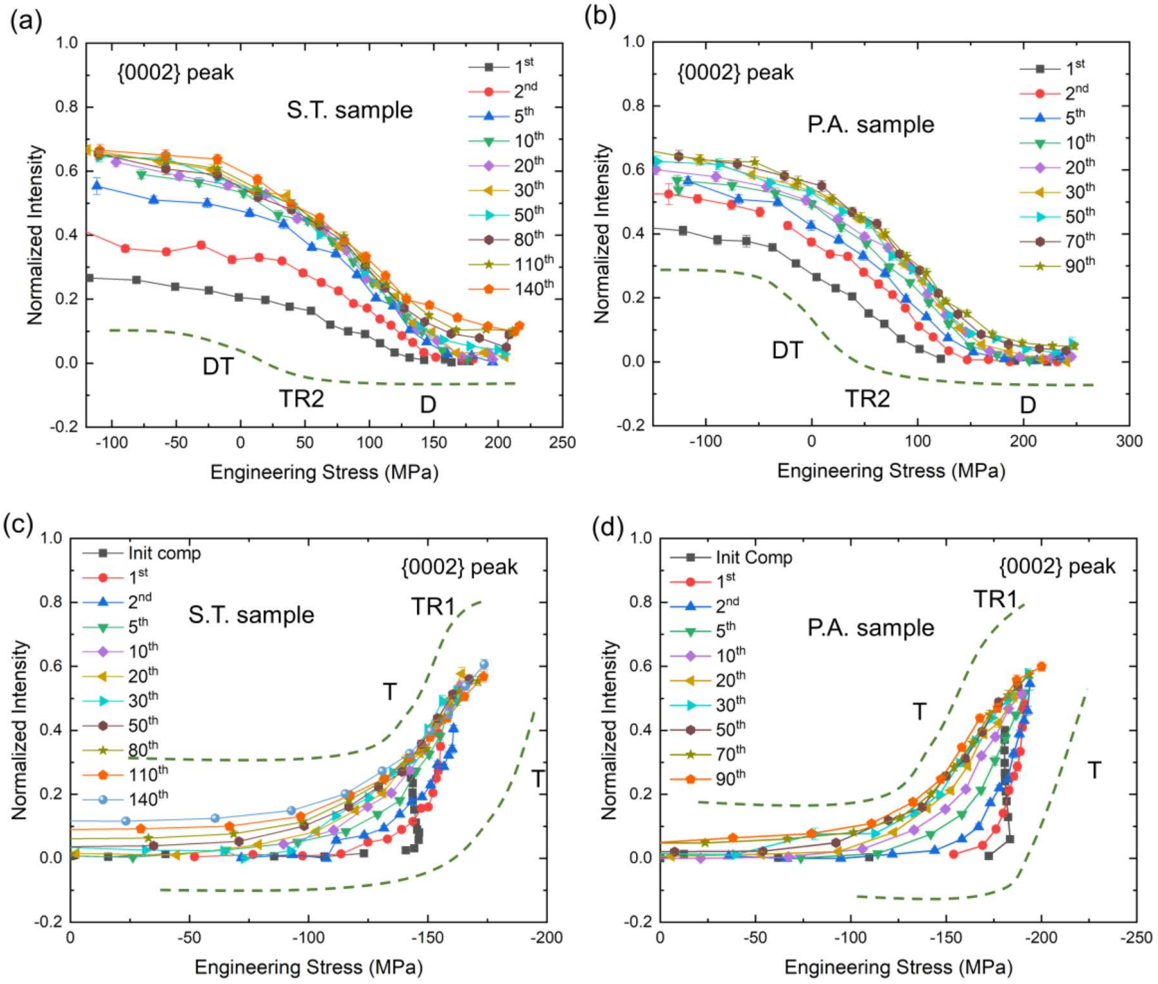

Fig. 4. The diffraction peak intensity variation of {0002} grains in selected fatigue cycles for the S.T. and P.A. samples: (a) and (b) during tension; (c) and (d) during compression.

sample, as displayed in Figs. 5(a) and 5(b). After the activation of extension twinning, the {0002} grains appear, and simultaneously the $\{10\bar{1}0\}$ grains yield directly in both the S.T. and P.A. samples. However, some differences are observed. First, the stress for the activation of extension twinning in the P.A. sample (∼ 181 MPa) is much higher than that in the S.T. sample (∼ 143 MPa). Second, the lattice strain of the {0002} twin grains at a macroscopic strain of -1% in the P.A. sample is much less than that in the S.T. sample, which is more easily noticed in Figs. 5(c) and 5(d) during unlading in the first cycle. The presence of non-zero lattice strains in selected grain orientations at zero stress can be attributed to the incomplete reversibility of plastic deformations in the initial compression process, which is consistence with the residual strain at zero stress observed in the macroscopic stress-strain curve in Fig. 2. When the samples are unloaded to 0 MPa after compression, the {0002} grains show a relatively large compressive residual strain, ∼ -765 με, in the S.T. sample, while a significant tensile residual strain in the P.A. sample, ∼ 1,250 με, in the parallel detector bank. This trend can be explained by the fact that a relatively large compressive lattice strain, ∼ -3,230 με, is accumulated in the {0002} twin grains during compression in the S.T. sample, as shown in Fig. 5(c), resulting in the remains of a certain amount of compressive residual strains after rapid unloading.

During the reverse tension in the 1st cycle, the plastic deformation is dominated by detwinning, DT, a transition from detwinning to dislocation, TR2, and dislocation motion, D, sequentially, in the S.T. and P.A. samples. The lattice strain responses in various groups of grains in different deformation stages are dissimilar in the axial direction in Figs. 5(e) and 5(f). Upon tension in the detwinning-dominated region, DT, the lattice strain increases rapidly in the $\{10\bar{1}0\}$ and $\{11\bar{2}0\}$ grains and slowly in the {0002} grains in the axial direction in the S.T. sample. In the transition from the detwinning to dislocation-dominated region, TR2, the $\{10\bar{1}1\}$ grains diverge vertically, and the {0002} grains gradually disappear in the axial direction, accompanying the recovery of $\{10\bar{1}0\}$ and $\{11\bar{2}0\}$ peak intensities and the decrease of the {0002} peak intensity to 0 in Fig. 3. The dislocation-controlled region, D, can also be divided into two regions corresponding to different microscopic strain responses. In the axial direction, the $\{10\bar{1}1\}$ grains depart from the linear response to the left in the dislocation region, D1, while both the $\{10\bar{1}1\}$ and $\{11\bar{2}0\}$ internal strain curves show a strong inflection at the macroscopic yield stress of ∼ 142 MPa in the dislocation-controlled region, D2. The lattice strain evolution in the P.A. sample is identical to that in the S.T. sample. The difference mainly lies in the much higher stress level (∼ 210 MPa) for the onset of the dislocation-controlled region, D2, in the P.A. sample in Fig. 5(f).

During compression in the first cycle, the general trends of the lattice-strain evolution in the S.T. and P.A. samples in Figs. 5(g) and 5(h) are similar to the initial compression in Figs. 5(a) and 5(b), respectively. It is noted that unlike the stress response in the initial compression after the activation of extension twinning where almost no work hardening is observed, the macroscopic stress still increases with the lattice strain accumulation during compression in the twinning-controlled region, T, in the first cycle. The lattice strain variations of different groups of grains for both the S.T. sample in the 80th cycle and the P.A. sample in the 70th

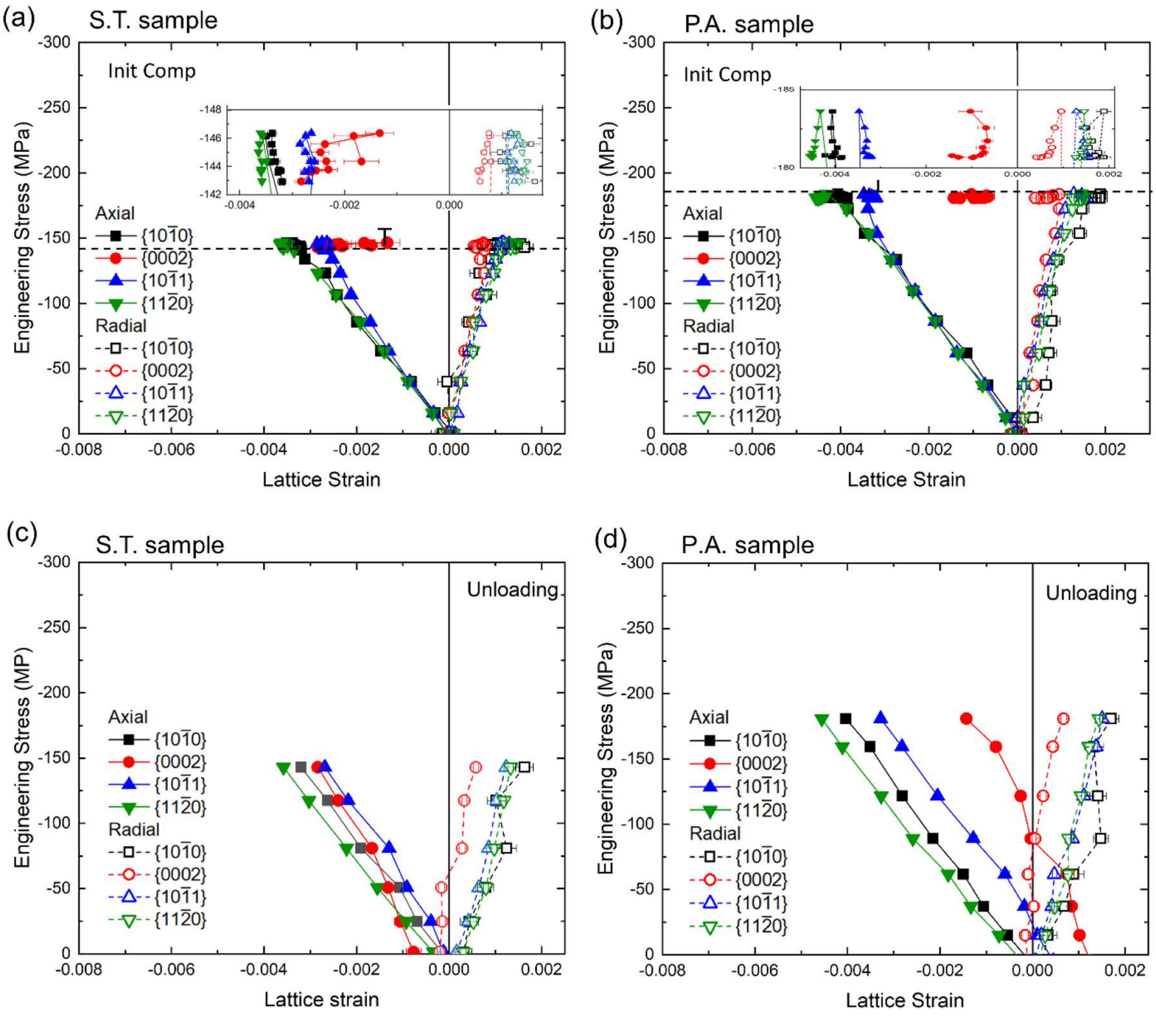

Fig. 5. Lattice strain evolution of certain interested hkils in selected fatigue cycles: the initial compression (a) and unloading from initial compression (c), the reverse tension (e) and compression (g) in the 1st cycle, and the reverse tension (i) and compression (k) in the 80th cycle for S.T. sample; the initial compression (b) and unloading from initial compression (d), the reverse tension (f) and compression (h) in the 1st cycle, and the reverse tension (j) and compression (l) in the 70th cycle for P.A. sample.

cycle are demonstrated in Figs. 5(i)-(l), which are identical to those in the first cycle in both S.T. and P.A. samples. It is worth mentioning that the lattice strain of the $\{0002\}$ grains exists in the entire tension process, suggesting the development of residual twins in these two samples. Different from the solely twinning-dominated plastic deformation in the 1st cycle during compression, the lattice strains evolved from the twinning region, T, to the transition from the twinning to dislocation region, TR1, in the 80th cycle in the S.T. sample and the 70th cycle in the P.A. sample. In the transition region, TR, the dislocation slip becomes more activated and the twinning/detwinning process becomes less significant, resulting in the that $\{0002\}$ grains that are in the poor orientation for the dislocation slip are relatively less relaxed and begin to share more portion of loads.

3.3. Microstructure evolution

Fig. 6(a) shows the EBSD inverse pole figure (IPF) maps and (0002) pole figures obtained from the solution-treated sample. Note that they were obtained from the plane perpendicular to the extrusion direction. The solution-treated sample has an average grain size of ~ 8.6 μm with the [0001] direction of most grains aligned to the radial direction of the extruded bar, which is a typically observed texture in extruded Mg alloys. Fig. 6(b) shows the HAADF-STEM image and selected area electron diffraction (SAED) pattern of the P.A. sample with the incident beam parallel to the zone axis of $[1\bar{1}00]_\alpha$. The fine plate-like precipitates that are densely distributed on the $(0002)_\alpha$, recognized as brightly imaged contrast, are identified as the G.P. zones according to the continuous streaks along the $[0001]_\alpha$ at the $1/3(11\bar{2}0)_\alpha$ and $2/3(11\bar{2}0)_\alpha$ positions in the $[1\bar{1}00]_\alpha$ SAED pattern. Close inspection of the high-magnification HAADF-STEM image reveals that these G.P. zones have a monolayer structure and provide a fully coherent interface with the Mg matrix as indicated by arrows in Fig. 6(c).

Fig. 7(a) shows EBSD IPF maps of the S.T. sample interrupted at the 30th fatigue cycle with a compression strain of 1%. A large number of lamella-shaped regions with distinct colors (boundaries highlighted in white) are formed in the parent grains. The misorientation angle distribution in Fig. 7(c) shows a high peak at 86°, indicating that these lamella-shaped regions are $\{10\bar{1}2\}$ tension twins (86.3° $<11\bar{2}0>$). The area fraction of tension twins in the 30-cycle S.T. sample is ~ 5.8% and reduced to ~ 2.3% after 177 cycles in a tension state, as displayed in Fig. 7(b). The number fraction of the 86° misorientation angle is also decreased to ~18.5% compared to that of the 30-cycle sample, ~34.4%, which suggests the occurrence of detwinning. The detwinned regions (boundaries highlighted in red) show similar colors as the parent grains, which suggests that both the detwinned region and the parent grain

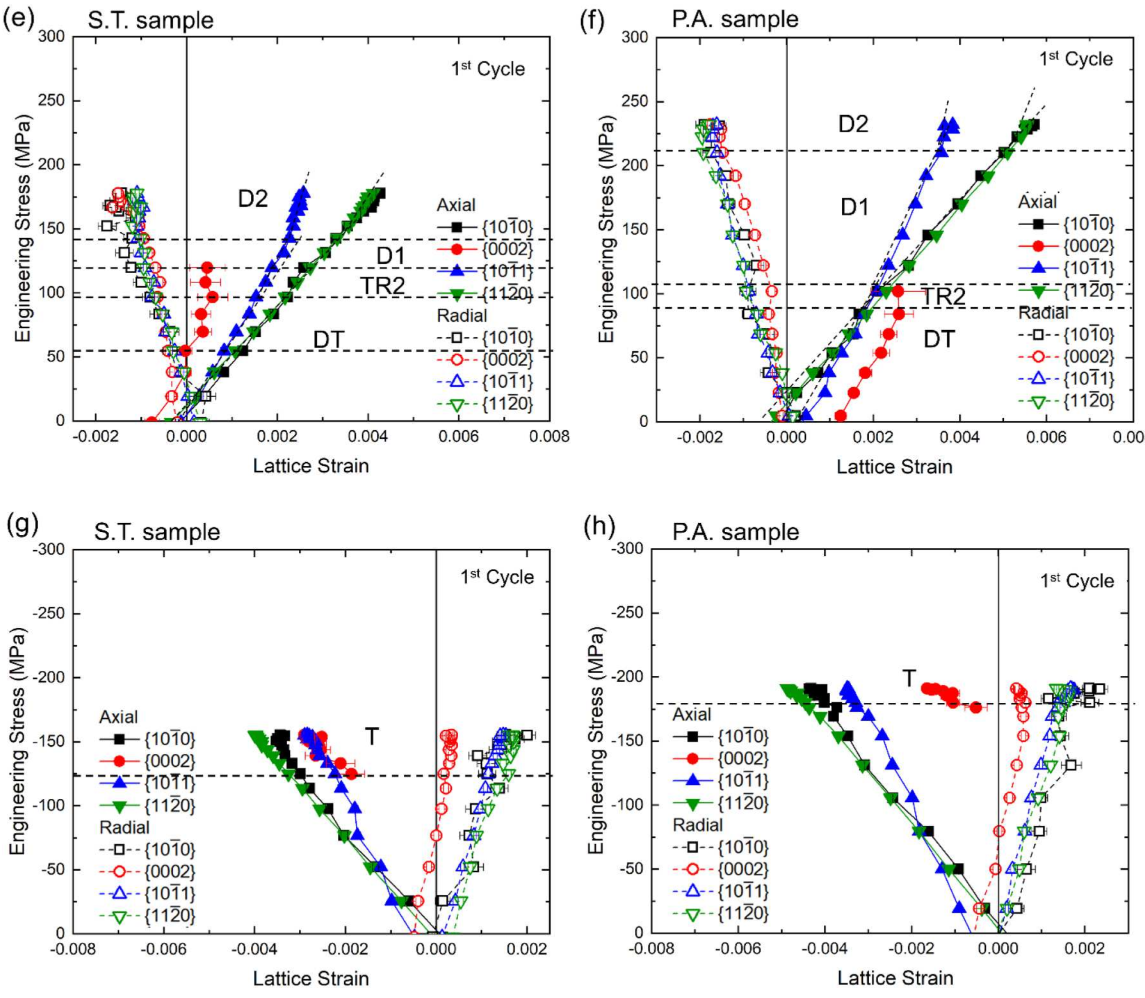

Fig. 5. (*continued*).

have similar orientations [34]. Unlike the S.T. sample, the activation of tension twins in the P.A. sample is suppressed during compression fatigue cycles, as demonstrated in the IPF maps in Fig. 7(d). The area fraction of tension twins, ~ 2.8% is lower than that of the solution-treated sample, ~ 5.8%, as shown in Fig. 7(f). After 108 cycles interrupted in a tension state, the areal fraction of tension twins is further decreased to only ~ 0.4%, while a large number of detwinned regions are detected within the parent grains, see Fig. 7(e).

Fig. 8(a) shows the low-magnification bright-field STEM (BF-STEM) image of the 30-cycle S.T. sample taken from the zone axis of $[11\bar{2}0]$. Abundant dislocations are observed in both the matrix and twin. The dislocation density near the twin boundaries (TBs) is high compared to that in the matrix, suggesting the dislocation pile-ups at TBs. Coarse rod-shaped and plate-shaped precipitates within the grain and along the TBs are considered as Al-Mn and Al-Ca phases as reported previously [7,9]. Figs. 8(b) and 8(c) show magnified two-beam BF-STEM images near the twin boundary under different diffraction vectors. Dislocation segments in the matrix are invisible under $g = [0002]$ but visible under $g = [1\bar{1}01]$, indicating that all the dislocations are $\langle a\rangle$-type dislocations. The $\langle a\rangle$ dislocations extend from the (0002) basal plane traces to non-basal ones, which suggests that dislocation cross-slip frequently occurs during cyclic deformation. In contrast, the P.A. sample shows a higher dislocation density and stronger dislocation pile-ups at the TBs after 30 fatigue cycles, see Fig. 8(d). The two beam images under different g vectors show that $\langle a\rangle$ dislocations are also dominant in the matrix, see Figs. 8(e) and 8(f). A large number of dislocation loops, however, are observed around tangled dislocation segments, indicating that dislocations are expected to bypass the G.P. zones via the Orowan process.

Fig. 9(a) shows the low-magnification BF-STEM image of the 177-cycle S.T. sample taken from the zone axis of $[11\bar{2}0]$. In comparison with the 30-cycle sample in a compression state, a discrete boundary (indicated by arrows) is clearly observed between the matrix and twin. Because the orientation of the basal plane is almost the same on both sides of the boundary, the left side of the boundary near the twin is considered to be the detwinned region. Figs. 9(b) and 9(c) exhibit the magnified images near the detwinned boundary under different g vectors. The dislocations that appear under $g = [0002]$ contain a $\langle c\rangle$ component in the Burgers vector, while the $\langle a\rangle$ dislocations are only visible under $g = [1\bar{1}01]$. In contrast, the P.A. sample shows much stronger dislocation pile-ups at both twin and detwinned boundaries after 108 fatigue cycles, see Fig. 9(d). The two-beam image under $g = [0002]$ in Fig. 9(e) indicates that these dislocation pile-ups are mainly $\langle c\rangle$-component dislocations as reported previously in Ref. [34–36]. Besides, a high density of $\langle a\rangle$-type dislocation tangles and loops are observed around the boundaries in Fig. 9(f).

The EBSD and STEM observations show distinctly different deformation behaviors between the S.T. and P.A. samples during cyclic fatigue, as illustrated in the schematic of the microstructural evolution upon the compression process in Fig. 10. Before the cyclic deformation, the P.A. sample contains a large number of G.P. zones lying on the basal planes of the matrix, see Fig. 10(d). Subsequent compressive loading leads to the activation of tensile twins and cross-slip of $\langle a\rangle$ dislocations in the S.T. sample, as shown in Fig. 10(b). However, the twin propagation is suppressed in the P.A. sample due to a large number of Orowan loops

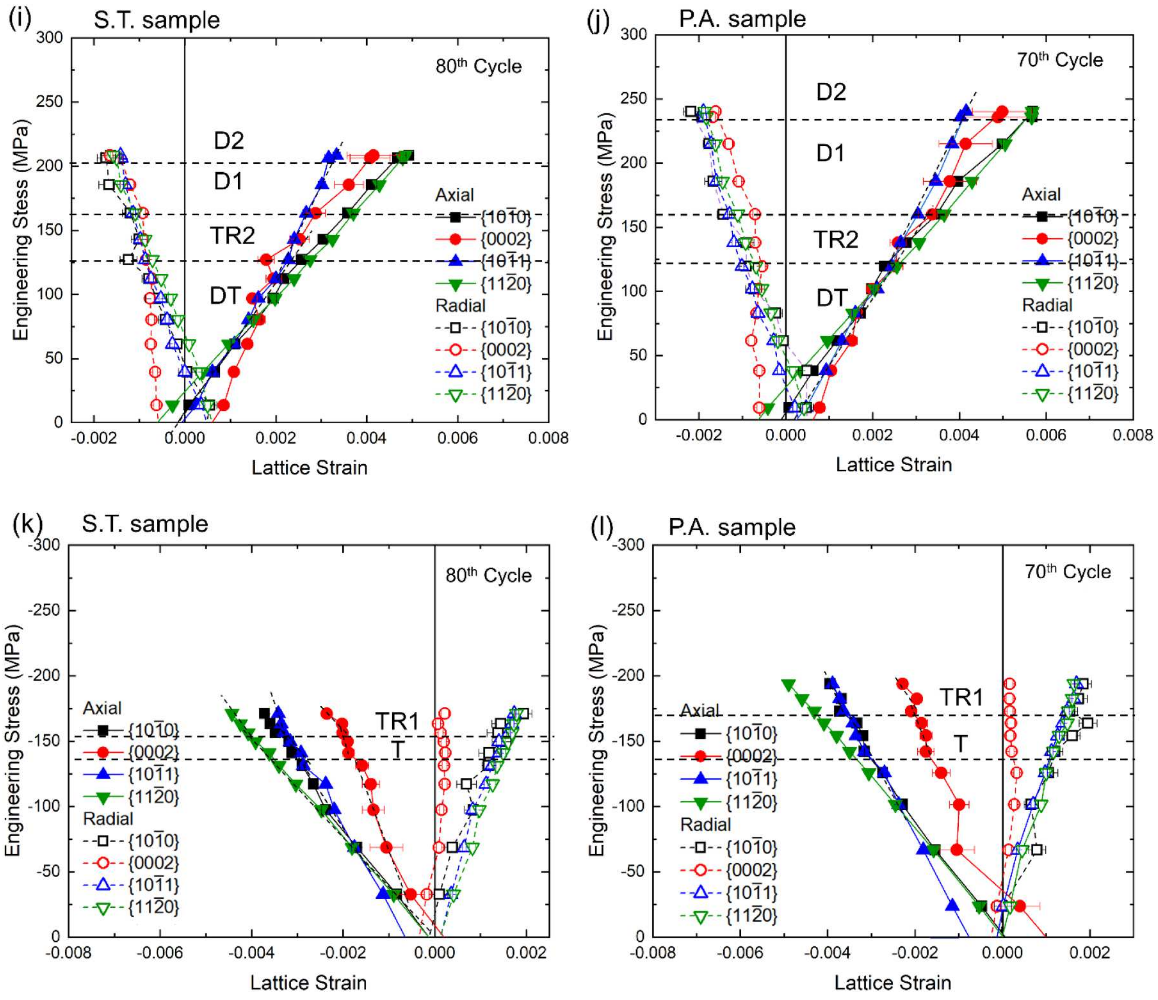

Fig. 5. (*continued*).

formation in the matrix, leading to intense dislocation pile-ups at twin boundaries, see Fig. 10(e). The detwinning occurs upon further tension loading with the twin significantly shrinking in the S.T. sample, see Fig. 10(c). The interaction between the dislocations and twin boundaries results in the formation of ⟨*c*⟩-component dislocations on the detwinned boundary. In contrast, a higher density of ⟨*c*⟩-component dislocations are formed in the P.A. sample due to the enhanced interaction between dislocation loops and detwinned boundaries, as displayed in Fig. 10(f). The tangling of mobile dislocations with pre-existing dislocation loops also increases the dislocation density near the twin boundary. Therefore, stronger dislocation pile-ups occur at both twin and detwinned boundaries.

Based on the TEM results, we can conclude that the higher strain-hardening rate of the P.A. sample during the reverse tension is attributed to the extra storage of dislocation loops formed by Orowan looping, and the smaller cyclic-hardening increment of the P.A. sample is also due to the slip irreversibility of dislocation loops, which shortens the slipping distance of primary dislocations, and thus leading to the rapid saturation of the dislocation density at the grain interior. Surprisingly, a large number of dislocation loops are formed during cyclic deformation, while the nanoscale coherent G.P. zones are generally favorable to be cut by dislocations rather than bypassed by the Orowan looping mechanism [37]. One possible explanation is that the <a> dislocations may dissociate into partials lying on the basal plane during the cyclic deformation [38], and then the “leading partial cutting with trailing partial looping” mechanism leads to the formation of dislocation loops [39–41]. However, further experiments on in-situ TEM observations and atomistic simulations would be required to understand this phenomenon in more detail.

4. Discussions

4.1. Deformation mechanisms

Generally, the overall deformation mechanism evolution in the S.T. sample is similar to that in the P.A. sample over fatigue cycles, which are elaborated in Fig. 11(a). The T, TR1, DT, TR2, D1, and D2-dominated regions are distinguished by different colors. The dividing points of these region boundaries are determined by the combination of lattice strain evolutions in certain interested hkils reflections (such as Fig. 5) and the diffraction intensity evolution of (0002) grains in each selected fatigue cycle (see Fig. 4). The compressive plastic deformation is controlled by the twinning process. The transition from the twinning to dislocation-dominated region, TR1, appeared since the 5th cycle in the S.T. sample and the 10th cycle in the P.A. sample, which tends to expand over fatigue cycles in Fig. 11(b). Although twinning is still the dominant deformation mode in the TR1 region, the dislocation motion becomes more active, resulting in a small extent of work hardening observed in this region. During reverse tension, the plastic deformation is initially predominated by the detwinning process, DT. The easy activation for detwinning can be ascribed to the fact that nucleation is not needed for detwinning [42]. In the transition from the detwinning to a dislocation-dominated region, TR2, the detwinning process gradually becomes exhausted and the dislocation slip turns out to be more and

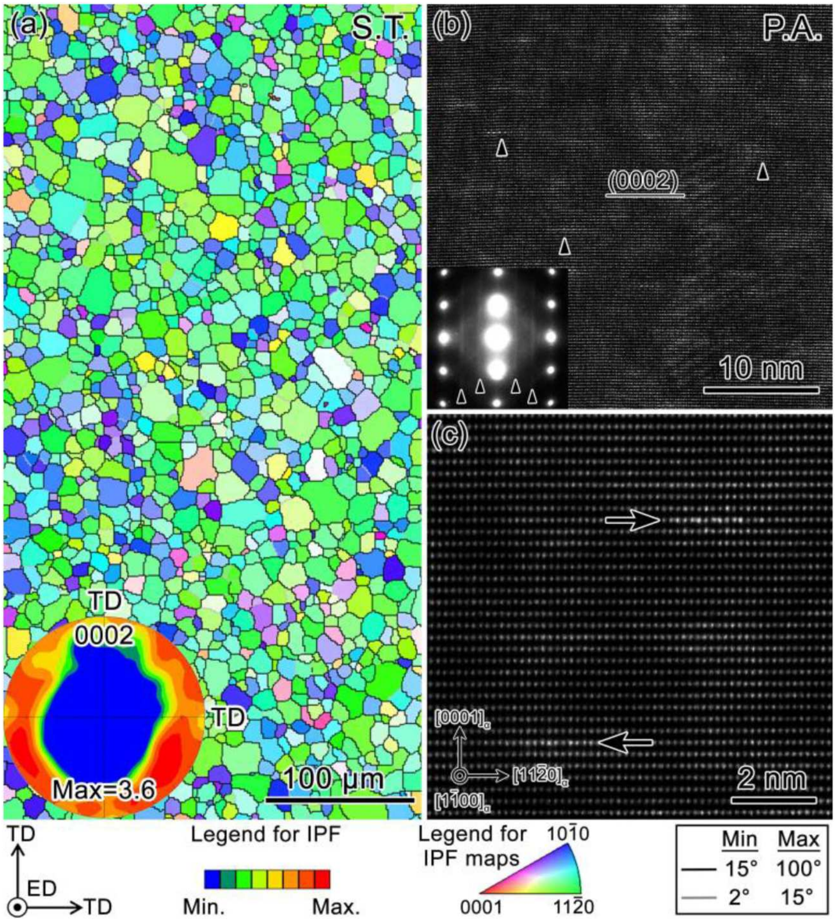

Fig. 6. (a) The EBSD IPF map and inverse pole figure of the solution-treated (S.T.) sample. (b) HAADF-STEM image and SAED pattern, and (c) atomic resolution image of the peak-aged (P.A.) sample. Note that the TEM image and SAED pattern are taken along the $[1\bar{1}00]_\alpha$ zone axis.

more active. It is obvious to note that the range of the dislocation-controlled region, D1, in the P.A. sample is much larger than that in the S.T. sample. In the dislocation-controlled region, D2, both two samples reached the second macro-yield in tension. Since the tensile yield strength of extrusions is mainly controlled by the prismatic slip based on the initial fiber texture [43], the dislocation-controlled region, D2, is proposed to be dominated by the prismatic slips, although $\langle c \rangle$-component dislocations are also observed, as shown in Fig. 9. As the basal slip has the lowest critical resolved shear stress (CRSS) of all the commonly observed deformation modes [17], it is reasonable to deduce that the dislocation motion in the transition region, TR2, and dislocation-controlled region, D1, is dominated by the basal <a> slip. It is worth noting that residual twins gradually develop since the 20th cycle in the S.T. sample and the 50th cycle in the P.A. sample. This fact suggested that the $\{10\bar{1}2\}$ twinning is not completely reversible during strain-controlled cyclic loading, which is also verified by Fig. 9. The accumulation of residual twins can act as a source of strain hardening by blocking the dislocation motion and also providing sites for crack initiation during fatigue [44].

4.2. Precipitate Strengthening

The high strength observed in the P.A. alloy is due to the dispersion of ordered G.P. zones lying on the (00.1) planes within the grains [7]. It is further interesting to discuss the effect of precipitates on the major slip systems and extension twinning. It is worth pointing out that all the following discussions are based on neutron diffraction data obtained from the axial detector bank. The deformation modes in the Mg alloy are generally affected by the initial textures (or grain orientation), which is essentially related to the Schmid factor [17,32]. Generally, deformation mechanisms in magnesium alloys include the basal slip, prismatic slip, pyramidal slips, and two twinning modes of $\{10\bar{1}2\}$ extension twinning and $\{10\bar{1}1\}$ contraction twinning [17]. In the current work, the pyramidal slips and compression twinning are not considered, as the pyramidal slip is mainly activated at high temperatures, and compression twinning usually occurs at large plastic deformations [17]. According to the Schmid law, τ_{CRSS} can be calculated by the following relation [23]:

$$\tau_{CRSS} = \sigma_c cos\lambda cos\varphi \tag{2}$$

where λ and ϕ are the angles between the loading directions and the slip (or twinning) plane normal and slip (or twinning) direction, respectively, and σ_c is the critical applied stress. The Schmid factors of the major slips and extension twinning for the $\{10\bar{1}0\}$, $\{11\bar{2}0\}$, and $\{10\bar{1}1\}$ grain orientations under uniaxial compression are listed in Table 1. According to the intensity variation in {0002} grains upon the initial compression, the initiation of twinning is detected at ~ 143 MPa in the S.T. sample and ~ 181 MPa in the P.A. sample, as shown in Figs. 5(a) and 5(b). According to Eq. (2), the CRSS values of ~ 71 ± 5 MPa and ~ 90 ± 7 MPa are calculated for the activation of extension twinning in the S.T. and the P.A. samples, respectively, with a maximum Schmid factor of 0.499, which suggests that the extension twinning is ~ 27% strengthened by the peak-aged treatment.

Since the $\{10\bar{1}1\}$ family is favorably oriented for the basal slip with the largest Schmid factor of 0.36, the CRSS for basal slip is estimated by the strain inflection of $\{10\bar{1}1\}$ grains upon initial compression. According to the stress level where the initial inflection in the $\{10\bar{1}1\}$ internal strain occurs (~ 36 MPa for the S.T. sample, and ~ 40 MPa for the

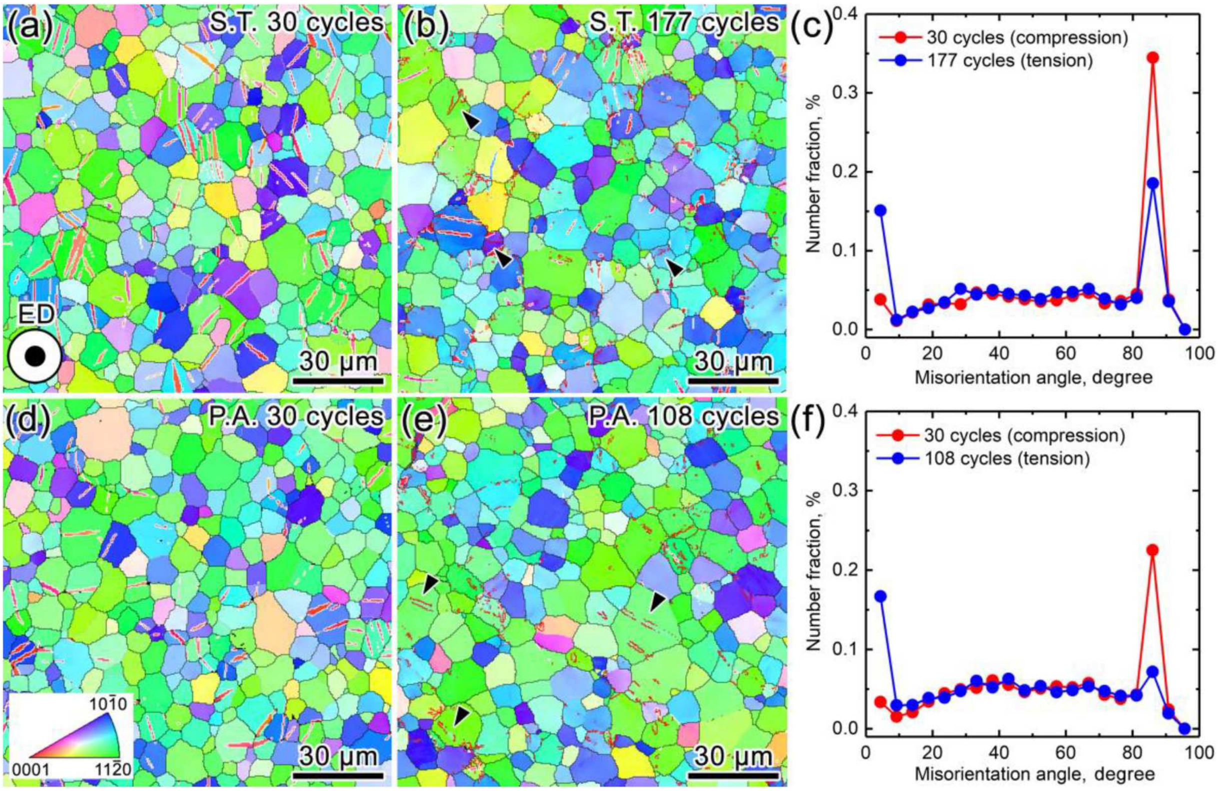

Fig. 7. EBSD IPF maps and misorientation angle distributions of (a-c) solution-treated (S.T.) and (d-f) peak-aged (P.A.) samples at the 30th fatigue cycle and near fatigue fracture.

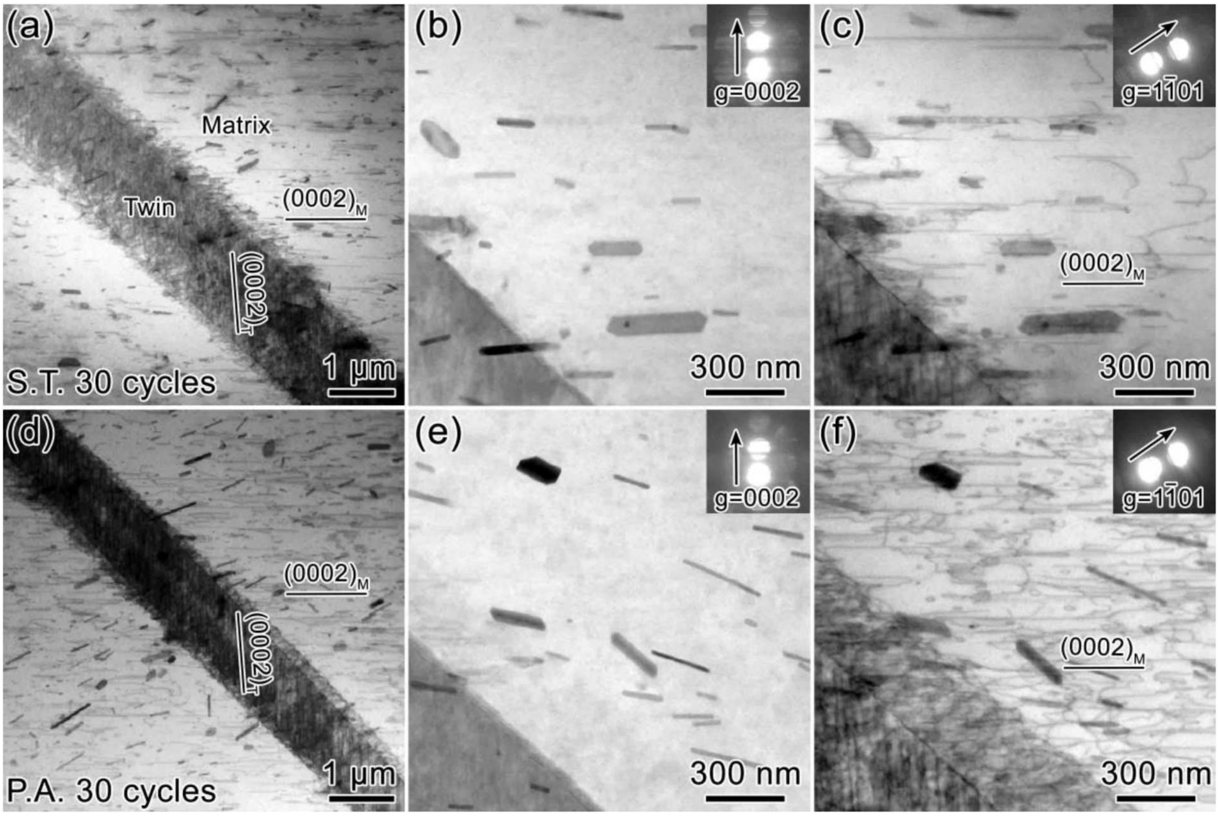

Fig. 8. BF-STEM images of (a-c) solution-treated (S.T.), and (d-f) peak-aged (P.A.) samples, both at 30 fatigue cycles. Note that the incident beam in (a) and (d) is parallel to the [11$\bar{2}$0] zone axis of the matrix. (b,c) and (e,f) were taken under different diffraction vectors, respectively.

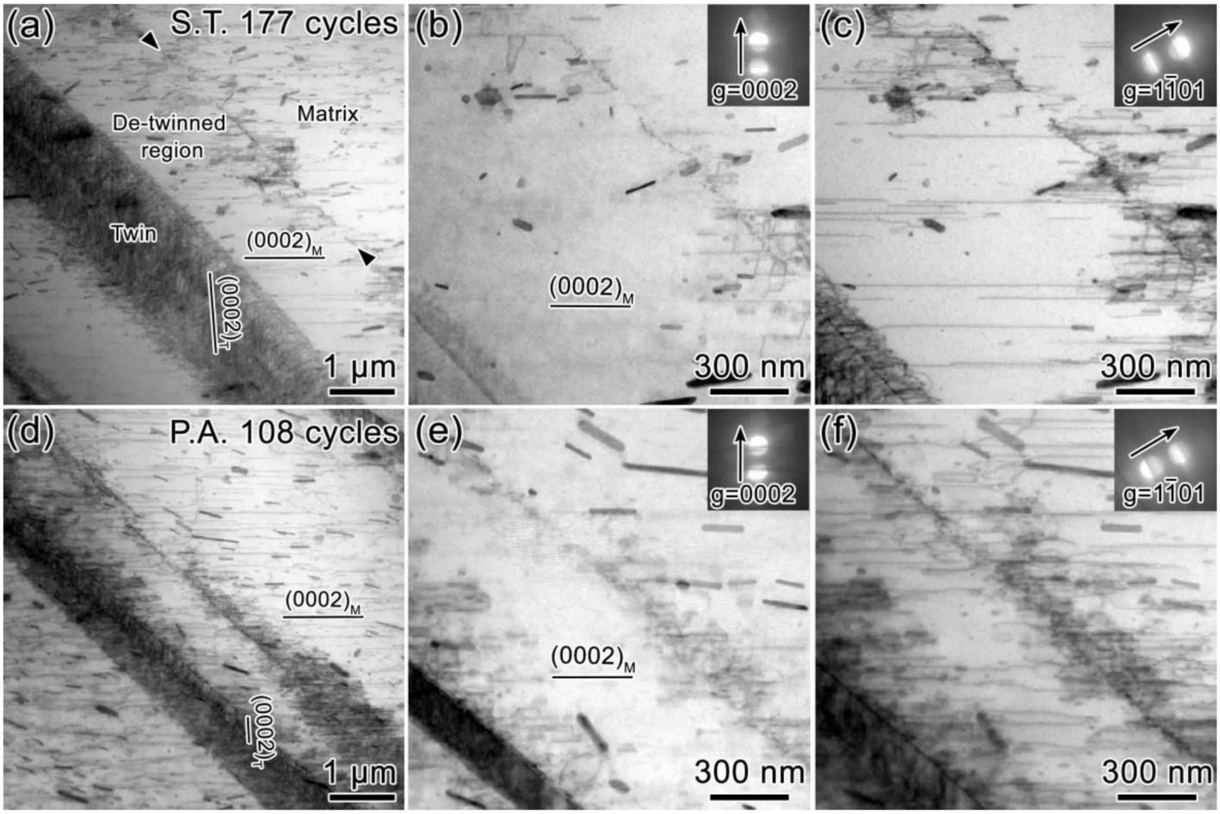

Fig. 9. BF-STEM images of (a-c) solution-treated (S.T.), and (d-f) peak-aged (P.A.) samples at 177 and 108 fatigue cycles, respectively. Note that the incident beam in (a) and (d) is parallel to the [11$\bar{2}$0] zone axis of the matrix. (b,c) and (e,f) were taken under different diffraction vectors, respectively.

P.A. sample) in Figs. 5(a) and 5(b), the calculated CRSS for basal slip is estimated to be 13 ± 5 MPa and ∼ 14.5 ± 5 MPa for the S.T. and P.A. samples, respectively. The basal <a> slip mode is strengthened (an ∼ 11% increase) over the solute-treatment state by the presence of fine plate-like G.P. zones in the peak-aged condition. However, it should be pointed out that the increment of the CRSS value for basal slip is in the error range. Notably, the age-hardening effect is also observed on the prismatic slip that is associated with the macroscopic tensile yield stress in the extruded Mg alloys [43]. Similar to the determination of the CRSS for basal slip, the critical stress for the activation of the prismatic slip is evaluated by the inflection point in the {11$\bar{2}$0} grains at ∼ 142 MPa in the S.T. sample and ∼ 210 MPa in the P.A. samples in Figs. 5(e) and 5(f), respectively. According to the maximum Schmid factor of 0.433 in {11$\bar{2}$0} grains, the CRSS value for the prismatic slip is ∼ 61 ± 6 MPa in the S.T. sample and 91 ± 5 MPa in the P.A. sample, reflecting a significant increase of approximately 49% in the P.A. sample's resistance to prismatic slip activation compared to the S.T. sample. The CRSS of the basal slip, prismatic slip, and extension twinning modes based on the Schmid law are summarized in Table 2. The hardening effect of G.P. zones lying on the (0001) planes provided the greatest strengthening against the prismatic slip, and the least to the basal slip, which is similar to the strengthening effect of the semi-coherent or incoherent basal plate-shaped precipitates [16].

The CRSS of the extension twinning and prismatic slip as a function of fatigue cycles for the S.T. and P.A. samples is presented in Fig. 12. Generally, the CRSS values for the extension twinning and prismatic slip in the P.A. sample are higher than those in the S.T. sample in all these fatigue cycles. With the increase in fatigue cycle, the CRSS value for prismatic slip gradually increases in both samples, suggesting the cyclic-hardening effect derived from the increased dislocation-dislocation interaction (work hardening) with increasing fatigue cycles, while the CRSS value for extension twinning in the P.A. rapidly decreased in the first 30 cycles and then almost kept stable in the rest cycles. It is interesting to notice that the CRSS value for extension twinning in the P.A. gradually approaches the near-stable value in the S.T. sample (see Fig. 12), which indicate the precipitation-strengthening effect on the twin onset gradually diminishes with fatigue cycles.

Robson et al. [45] proposed that precipitates do not strongly suppress the nucleation of the extension twinning in Mg and its alloys, but impede the propagation and growth processes. It is interesting to note the lattice strains, e_{0002}, at the first appearance of twinning reflection ({0002} grains) in the initial compression in the S.T. sample is larger than that in the P.A. sample, as shown in Figs. 5(a) and 5(b). This fact suggests the {0002} lattice stress at twin onset, also known as "twin internal stress", may differ due to aging treatment, which can be evaluated by $\sigma_{0002} = E_{0002}e_{0002}$, where E_{0002} is Young's modulus of the {0002} reflection. The {0002} lattice stress at the twin-onset evolution with the fatigue cycles of the S.T. and P.A. samples, marked by the hollow cycles, are summarized in Fig. 13, which almost keeps stable in the former one, and gradually increases in the latter one. Although the aging treatment increases the macro-stress level for the onset of twinning, the absolute value of the {0002} lattice stress at the twin onset dropped. A similar trend is reported by Kada et al. [46], who investigated the slip and twinning in the presence of precipitates in AZ91 alloy using in situ X-ray diffraction. As shown in Fig. 5(a) and Fig. 5(b), the twins are formed with internal stress lower than their parent grains and the surrounding polycrystalline aggregate. This has been well reported in previous studies [46–49]. The relatively high twin internal stress in the S.T. sample may be related to easier micro-slip associated with twin nucleation, which immediately relaxes high local stresses caused by the misfit between the twined grains and the surrounding aggregate [47]. It should be pointed out that the determination of lattice stress at the twin onset from pre-existing orientations should use the de-convoluted from the twin reflections [46]. In the current case, however, the {0002}

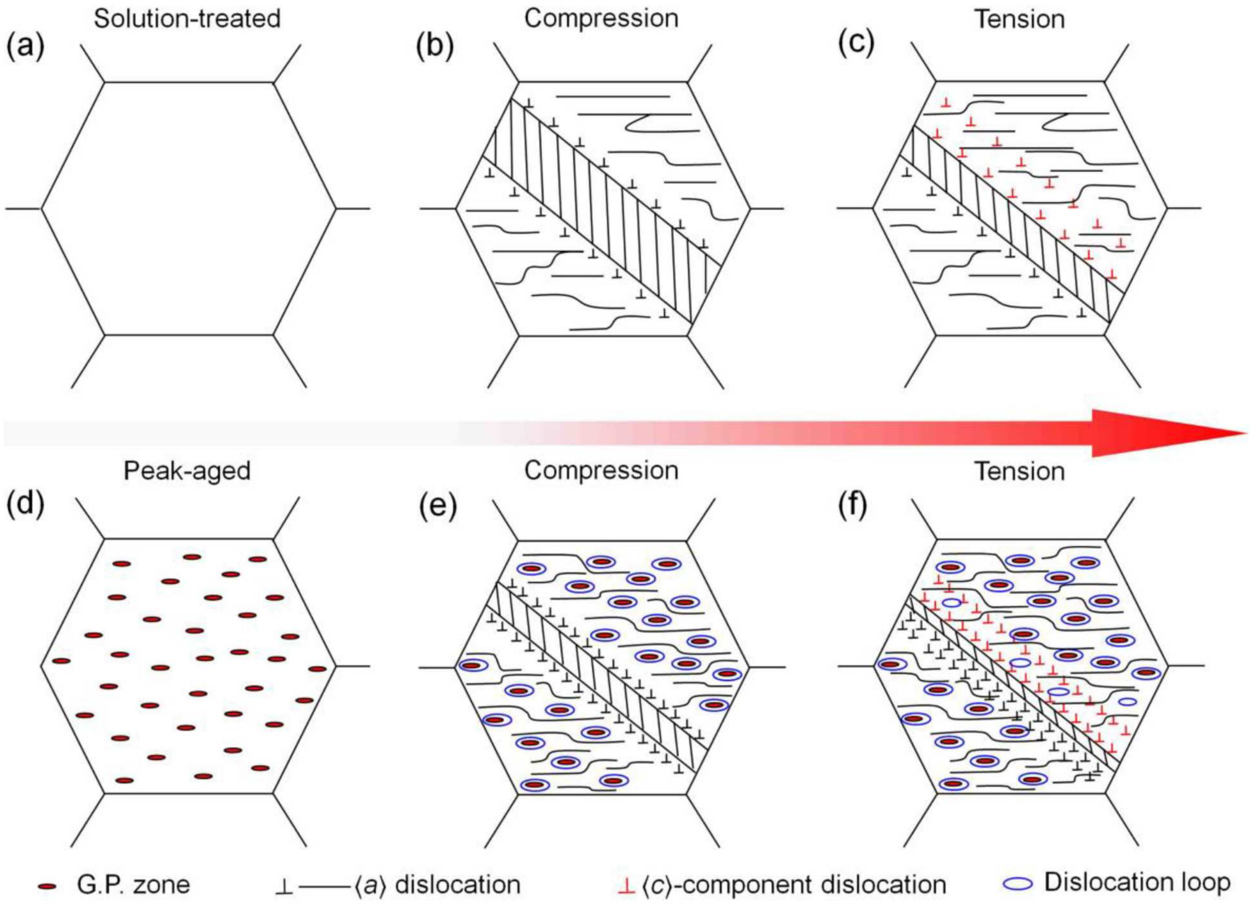

Fig. 10. Schematics illustrations of microstructural evolution in the (a-c) solution-treated (S.T.), and (d-f) peak-aged (P.A.) samples during cyclic fatigue process.

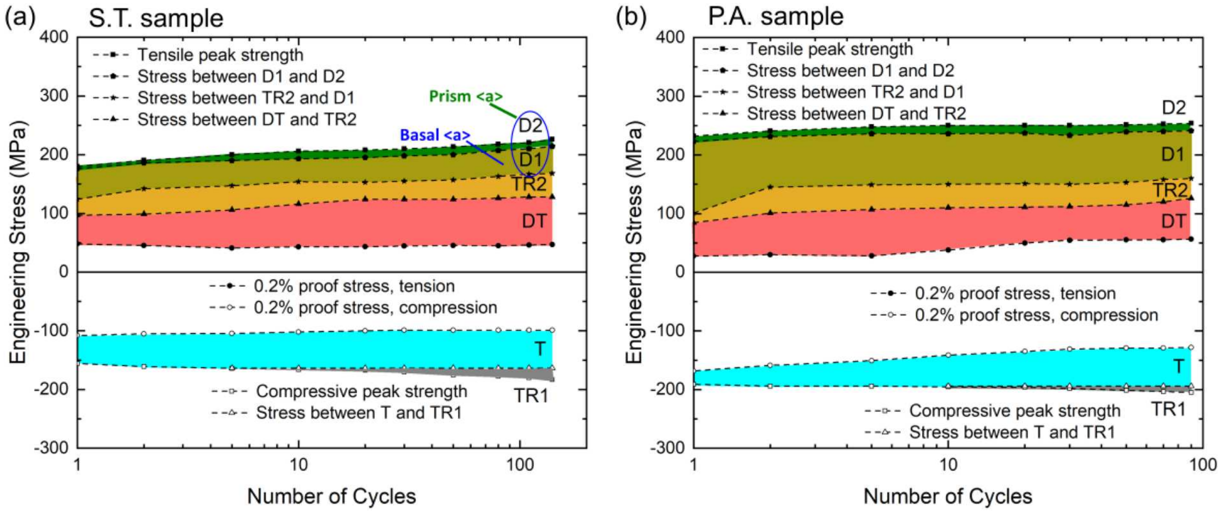

Fig. 11. Deformation modes, divided by the peak stress, 0.2% proof stress, stress at the dividing point among twinning/detwinning, transition region, dislocation region, as a function of fatigue cycles in (a) the S.T. sample and (b) the P.A. sample.

lattice stress at twin onset in each selected cycle is directly determined by the first appearance of {0002} twinning reflections (first the 50 cycles) or by the activation of the twinning-dominated region in the axial detector bank (after the 50 cycles) because of the low resolution of the current diffraction data. The local backstress, defined by the difference between the $\{10\bar{1}0\}$ twin parent stress and the {0002} lattice stress at twin onset, have been taken into consideration for the two samples, as displayed by solid circles in Fig. 13(a). It is clear to see that the twin backstress at the twin onset is higher in the P.A. sample than that in the S.T. sample during the whole fatigue life. However, the twin backstress significantly decreases in the first 30 cycles in the P.A. sample, bringing it close to that in the S.T. sample, and then almost remained constant in the following cycles. These observations suggest that the backstress difference caused by the aging treatment decreases as the fatigue cycles

Table 1
Schmid factors of the major slips and extension twinning for several grain orientations {hkil} in Mg alloys with the HCP structure under uniaxial compression.

Deformation mode	Reflection	$\{10\bar{1}0\}$	$\{10\bar{1}1\}$	$\{11\bar{2}0\}$
Extension Twinning	$(10\bar{1}2)[\bar{1}011]$	0.499	0.305	0.374
	$(01\bar{1}2)[0\bar{1}11]$	0.125	0	0.374
	$(\bar{1}102)[1\bar{1}01]$	0.125	-0.027	0
	$(\bar{1}012)[10\bar{1}1]$	0.499	0.251	0.374
	$(0\bar{1}12)[01\bar{1}1]$	0.125	-0.027	0.374
	$(1\bar{1}02)[\bar{1}101]$	0.125	0	0
	Max	0.499	0.305	0.374
Basal <a>	$(0001)[2\bar{1}\bar{1}0]$	0	-0.360	0
	$(0001)[\bar{1}2\bar{1}0]$	0	0	0
	$(0001)[\bar{1}\bar{1}20]$	0	0.360	0
	Max	0	0.360	0
Prismatic <a>	$(10\bar{1}0)[\bar{1}2\bar{1}0]$	0	0	-0.433
	$(0\bar{1}10)[2\bar{1}\bar{1}0]$	0.433	0.337	0.433
	$(\bar{1}100)[\bar{1}\bar{1}20]$	-0.433	-0.337	0
	Max	0.433	0.337	0.433

Table 2
CRSS of the major slips and extension twinning modes based on the Schmid law determined for the S.T. and P.A. samples in the initial compression and the 1st cycle.

Deformation Mode	S.T. (MPa)	P.A. (MPa)	Increase (%)
Basal <a>	13 ± 5	14.5 ± 5	~ 11
Prismatic <a>	61 ± 6	91 ± 5	~ 49
Extension Twinning	71 ± 5	90 ± 7	~ 27

progress.

Two pathways to explain how twins establish the backstress are proposed recently [46,50]. The first pathway assumes that the twin nucleates and propagates with a negligible thickness until being impeded by the grain boundaries, and then proceeds to thicken, which increases its aspect ratio and backstress [50]. The second one assumes that the twin nucleates and propagates with considerable (fixed) thickness until trapped by grain boundary or obstacles and establish its equilibrium aspect ratio [46]. The second pathway theory is adopted here to explain the high backstress in the P.A. sample. According to Eshelby's method, the backstress of a penny-shaped inclusion in Mg can be calculated using the equation $\tau_B = 2sqG$, where s is the twinning shear (0.13), q is the twin aspect ratio (thickness/length), and G is the shear modulus (~ 17 GPa) [46]. The propagation of twins in the P.A. sample is hindered by the precipitates shortly after leaving the region of stress concentration where it formed. This hindrance can lead to high backstress due to the relatively large twin aspect ratio. However, these G.P. zones in the P.A. sample can be gradually engulfed and consumed by twins [51–53] with cyclic loading, which will no longer provide significant resistance to the subsequent propagation of twins. In the following cycles, the twins with fixed thickness can propagate relatively long distances until they are held by other precipitates that have not been engulfed or even the perimeter of the grain boundaries. The schematic representation of twin propagation and growth in the P.A. sample with cyclic loading is shown in Fig. 13(b). The value of the aspect ratio will therefore drop rapidly in such a case, which leads to a considerable reduction in backstress in the P.A. sample, gradually bringing it closer to the backstress observed in the S.T. sample. This finding, combined with the analysis of CRSS evolution for twin onset, indicates the effect of the G.P zone on twin initiation and propagation in the P.A. reduces with fatigue cycles.

5. Conclusions

Deformation mechanisms of an extruded Mg alloy with the solution treatment (S.T.) and peak-aged treatment (P.A.) during the fully reversed strain-controlled low-cycle fatigue were systematically investigated by the *in situ* neutron diffraction technique and advanced characterization tools. The following conclusions can be drawn from the current work, as described below:

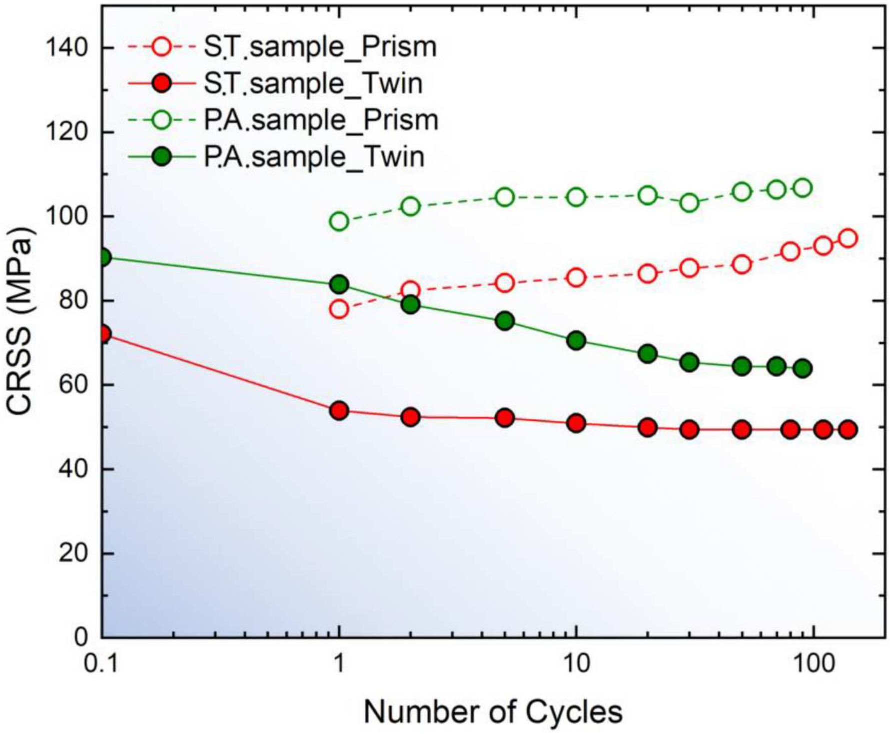

Fig. 12. The CRSS variation for the extension twinning and prismatic slip in the S.T. and P.A. samples over fatigue cycles.

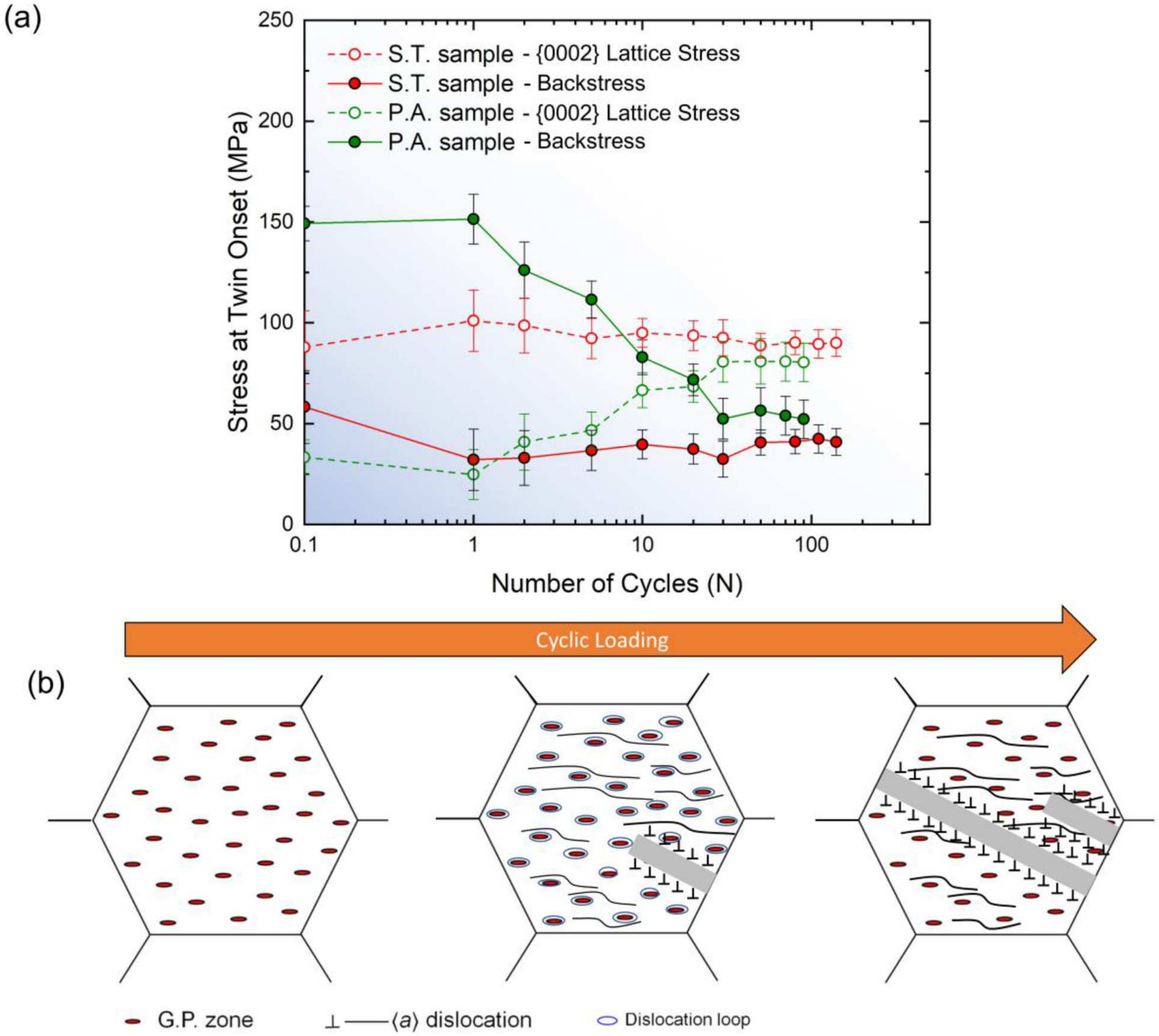

Fig. 13. (a) Lattice stress in the twin grains at the onset of twinning and the back stress (the difference between parent and twin stresses) as a function of fatigue cycles in the S.T. and P.A. samples. (b) Schematic representation of twin propagation and growth in the P.A. sample.

(1) The general deformation mechanism evolutions in the S.T. and P.A. samples were found to be similar in the sense that the deformation in compression relied on the extension twinning and the plastic deformation in tension was controlled by the detwinning, transition from the detwinning to dislocation, and dislocation motion, sequentially.
(2) The effect of G.P. zones on the strengthening of the major slips and extension twinning mode in the extruded magnesium has been discussed. The precipitation provided the greatest strengthening against the prismatic slip (∼ 49% increase), the moderate to $\{10\bar{1}2\}$ extension twinning (∼ 27 %), and the least to basal slip (∼ 11% increase).
(3) With the fatigue cycle going on, the strengthening effect of the G.P. zone gradually decreases, indicated by the decreased CRSS for the extension twinning and local backstress in the P.A. sample, which gradually approaches that in the S.T. sample.
(4) Under strain-controlled fatigue loading, a reduced fatigue life was observed in the P.A. sample, compared with the S.T. sample. This trend was attributed to the fact that the formation of pile-ups of <a> and <c+a> dislocations and the accumulation of higher back stress in the P.A. sample, both of which would promote the crack initiation.

Data availability

Data contained in this paper are available upon request to the corresponding authors.

Declaration of Competing Interest

The authors declare that they have no known competing financial interests or personal relationships that could have appeared to influence the work reported in this paper.

Acknowledgments

The present work is supported by the US National Science Foundation (DMR 1809640 & DMR 1809696), and also in-part by JSPS KAKENHI [Grant Number JP21H01675] and Element Strategy Initiative of MEXT [Grant Number JPMXP0112101000]. The neutron diffraction work was carried out at the Spallation Neutron Source (SNS), which is the U.S. Department of Energy (DOE) user facility at the Oak Ridge National Laboratory, sponsored by the Scientific User Facilities Division, Office of Basic Energy Sciences. The authors thank Dr. M. J. Frost at SNS for the technique support.

References

[1] B. Mordike, T. Ebert, Magnesium: properties-applications-potential, Mater. Sci. Eng., A 302 (2001) 37–45.

[2] Z. Yang, J. Li, J. Zhang, G.W. Lorimer, J. Robson, Review on research and development of magnesium alloys, Acta Metall. Sin. (Engl. Lett.) 21 (2009) 313–328.

[3] A.A. Luo, Recent magnesium alloy development for elevated temperature applications, Int. Mater. Rev. 49 (2013) 13–30.

[4] A. Luo, M.O. Pekguleryuz, Cast magnesium alloys for elevated temperature applications, J. Mater. Sci. 29 (1994) 5259–5271.

[5] X. Gao, S.M. Zhu, B.C. Muddle, J.F. Nie, Precipitation-hardened Mg-Ca-Zn alloys with superior creep resistance, Scr. Mater. 53 (2005) 1321–1326.

[6] A. Suzuki, N.D. Saddock, J.R. TerBush, B.R. Powell, J.W. Jones, T.M. Pollock, Precipitation strengthening of a Mg-Al-Ca–based AXJ530 die-cast alloy, Metall. Mater. Trans. A 39 (2008) 696–702.

[7] T. Nakata, C. Xu, R. Ajima, K. Shimizu, S. Hanaki, T.T. Sasaki, L. Ma, K. Hono, S. Kamado, Strong and ductile age-hardening Mg-Al-Ca-Mn alloy that can be extruded as fast as aluminum alloys, Acta Mater 130 (2017) 261–270.

[8] M. Cihova, R. Schäublin, L.B. Hauser, S.S.A. Gerstl, C. Simson, P.J. Uggowitzer, J.F. Löffler, Rational design of a lean magnesium-based alloy with high age-hardening response, Acta Mater 158 (2018) 214–229.

[9] M.Z. Bian, T.T. Sasaki, T. Nakata, Y. Yoshida, N. Kawabe, S. Kamado, K. Hono, Bake-hardenable Mg-Al-Zn-Mn-Ca sheet alloy processed by twin-roll casting, Acta Mater 158 (2018) 278–288.

[10] Z.H. Li, T.T. Sasaki, T. Shiroyama, A. Miura, K. Uchida, K. Hono, Simultaneous achievement of high thermal conductivity, high strength and formability in Mg-Zn-Ca-Zr sheet alloy, Mater. Res. Lett. 8 (2020) 335–340.

[11] R. Shi, J. Miao, T. Avey, A.A. Luo, A new magnesium sheet alloy with high tensile properties and room-temperature formability, Sci. Rep. 10 (2020) 10044.

[12] F. Kabirian, R. Mahmudi, Effects of rare earth element additions on the impression creep behavior of AZ91 magnesium alloy, Metall. Mater. Trans. A 40 (2009) 2190–2201.

[13] L. Liu, F. Yuan, M. Zhao, C. Gao, P. Feng, Y. Yang, S. Yang, C. Shuai, Rare earth element yttrium modified Mg-Al-Zn alloy: microstructure, degradation properties and hardness, Materials (Basel) 10 (2017) 477.

[14] W. Liu, F. Cao, L. Zhong, L. Zheng, B. Jia, Z. Zhang, J. Zhang, Influence of rare earth element Ce and La addition on corrosion behavior of AZ91 magnesium alloy, Mater. Corros. 60 (2009) 795–803.

[15] J.F. Nie, Effects of precipitate shape and orientation on dispersion strengthening in magnesium alloys, Scripta Mater 48 (2003) 1009–1015.

[16] J.D. Robson, N. Stanford, M.R. Barnett, Effect of precipitate shape and habit on mechanical asymmetry in magnesium alloys, Metall. Mater. Trans. A 44 (2012) 2984–2995.

[17] S.R. Agnew, R.P. Mulay, F.J. Polesak, C.A. Calhoun, J.J. Bhattacharyya, B. Clausen, In situ neutron diffraction and polycrystal plasticity modeling of a Mg-Y-Nd-Zr alloy: effects of precipitation on individual deformation mechanisms, Acta Mater 61 (2013) 3769–3780.

[18] J. Wang, N. Stanford, Investigation of precipitate hardening of slip and twinning in Mg5%Zn by micropillar compression, Acta Mater 100 (2015) 53–63.

[19] J.D. Robson, N. Stanford, M.R. Barnett, Effect of precipitate shape on slip and twinning in magnesium alloys, Acta Mater 59 (2011) 1945–1956.

[20] W. Wu, K. An, Understanding low-cycle fatigue life improvement mechanisms in a pre-twinned magnesium alloy, J. Alloys Compd. 656 (2016) 539–550.

[21] W. Wu, K. An, L. Huang, S.Y. Lee, P.K. Liaw, Deformation dynamics study of a wrought magnesium alloy by real-time in situ neutron diffraction, Scripta Mater 69 (2013) 358–361.

[22] H. Fan, Y. Zhu, J.A. El-Awady, D. Raabe, Precipitation hardening effects on extension twinning in magnesium alloys, Int. J. Plast. 106 (2018) 186–202.

[23] L. Wu, S.R. Agnew, D.W. Brown, G.M. Stoica, B. Clausen, A. Jain, D.E. Fielden, P.K. Liaw, Internal stress relaxation and load redistribution during the twinning–detwinning-dominated cyclic deformation of a wrought magnesium alloy, ZK60A, Acta Mater 56 (2008) 3699–3707.

[24] W. Wu, P.K. Liaw, K. An, Unraveling cyclic deformation mechanisms of a rolled magnesium alloy using in situ neutron diffraction, Acta Mater 85 (2015) 343–353.

[25] L. Wu, A. Jain, D.W. Brown, G.M. Stoica, S.R. Agnew, B. Clausen, D.E. Fielden, P.K. Liaw, Twinning–detwinning behavior during the strain-controlled low-cycle fatigue testing of a wrought magnesium alloy, ZK60A, Acta Mater 56 (2008) 688–695.

[26] W. Reimers, A.R. Pyzalla, A. Schreyer, H. Clemens, (eds) Neutrons and Synchrotron Radiation in Engineering Materials science, From Fundamentals to Material and Component Characterization (2008), John Wiley Inc.

[27] X.L. Wang, T.M. Holden, G.Q. Rennich, A.D. Stoica, P.K. Liaw, H. Choo, C.R. Hubbard, VULCAN - The engineering diffractometer at the SNS, Physica B: Condensed Matter 385-386 (2006) 673–675.

[28] P.K. Liaw, H. Choo, R.A. Buchanan, C.R. Hubbard, X.L. Wang, Development of an in situ neutron-scattering facility for research and education in the mechanical behavior of materials, Mater. Sci. Eng., A 437 (2006) 126–133.

[29] K. An, Y. Chen, A.D. Stoica, VULCAN: a "hammer" for high-temperature materials research, MRS Bulletin 44 (2019) 878–885.

[30] K. An, H.D. Skorpenske, A.D. Stoica, D. Ma, X.-.L. Wang, E. Cakmak, First in situ lattice strains measurements under load at VULCAN, Metall. Mater. Trans. A 42 (2010) 95–99.

[31] K. An, Data reduction and interactive visualization software for event mode neutron diffraction, ORNL Report (621) (2012). ORNL-TM-2012.

[32] D.W. Brown, S.R. Agnew, M.A.M. Bourke, T.M. Holden, S.C. Vogel, C.N. Tomé, Internal strain and texture evolution during deformation twinning in magnesium, Mater. Sci. Eng. A 399 (1–2) (2005) 1–12.

[33] D. Xie, W. Zhang, Z. Lyu, P.K. Liaw, H. Tran, H.B. Chew, Y.J. Wei, Y. Ren, Y.F. Gao, Plastic anisotropy and twin distributions near the fatigue crack tip of textured Mg alloys from in situ synchrotron x-ray diffraction measurements and multiscale mechanics modeling, J. Mech. Phys. Solids 165 (2022), 104936.

[34] W. Gong, R. Zheng, S. Harjo, T. Kawasaki, K. Aizawa, N. Tsuji, In-situ observation of twinning and detwinning in AZ31 alloy, J. Magnes. Alloy 12 (2022) 3418–3432.

[35] F. Wang, K. Hazeli, K.D. Molodov, C.D. Barrett, T. Al-Samman, D.A. Molodov, A. Kontsos, K.T. Ramesh, H. El Kadiri, S.R. Agnew, Characteristic dislocation substructure in 1012 twins in hexagonal metals, Scr. Mater. 143 (2018) 81–85.

[36] F. Wang, C.D. Barrett, R.J. McCabe, H. El Kadiri, L. Capolungo, S.R. Agnew, Dislocation induced twin growth and formation of basal stacking faults in {1012} twins in pure Mg, Acta Mater 165 (2019) 471–485.

[37] T. Gladman, Precipitation hardening in metals, Mater Sci Technol 15 (1999) 30–36.

[38] S.R. Agnew, J.A. Horton, M.H. Yoo, Transmission electron microscopy investigation of <c+a>dislocations in Mg and α-solid solution Mg-Li alloys, Metall. Mater. Trans. A 33 (2002) 851–858.

[39] C.V. Singh, D.H. Warner, Mechanisms of Guinier–Preston zone hardening in the athermal limit, Acta Mater 17 (2010) 5797–5805.

[40] C.V. Singh, A.J. Mateos, D.H. Warner, Atomistic simulations of dislocation–precipitate interactions emphasize importance of cross-slip, Scr. Mater. 5 (2011) 398–401.

[41] V.S. Krasnikov, A.E. Mayer, V.V. Pogorelko, F.T. Latypov, A.A. Ebel, Interaction of dislocation with GP zones or θ'' phase precipitates in aluminum: atomistic simulations and dislocation dynamics, Int. J. Plast. 125 (2020) 169–190.

[42] X. Lou, M. Li, R. Boger, S. Agnew, R. Wagoner, Hardening evolution of AZ31B Mg sheet, Int. J. Plast. 23 (2007) 44–86.

[43] S. Agnew, D. Brown, C. Tome, Validating a polycrystal model for the elastoplastic response of magnesium alloy AZ31 using in situ neutron diffraction, Acta Mater 54 (2006) 4841–4852.

[44] J. Koike, N. Fujiyama, D. Ando, Y. Sutou, Roles of deformation twinning and dislocation slip in the fatigue failure mechanism of AZ31 Mg alloys, Scripta Mater 63 (2010) 747–750.

[45] J.D. Robson, M.R. Barnett, The effect of precipitates on twinning in magnesium alloys, Adv. Eng. Mater. 21 (2019), 1800460.

[46] S.R. Kada, P.A. Lynch, J.A. Kimpton, M.R. Barnett, In-situ X-ray diffraction studies of slip and twinning in the presence of precipitates in AZ91 alloy, Acta Mater 119 (2016) 145–156.

[47] O. Muránsky, M.R. Barnett, D.G. Carr, S.C. Vogel, E.C. Oliver, Investigation of deformation twinning in a fine-grained and coarse-grained ZM20 Mg alloy: combined in situ neutron diffraction and acoustic emission, Acta Mater 58 (2010) 1503–1517.

[48] O. Muránsky, D.G. Carr, P. Šittner, E.C. Oliver, In situ neutron diffraction investigation of deformation twinning and pseudoelastic-like behaviour of extruded AZ31 magnesium alloy, Int. J. Plast. 25 (2009) 1107–1127.

[49] B. Clausen, C.N. Tome, D.W. Brown, S.R. Agnew, Reorientation and stress relaxation due to twinning: modeling and experimental characterization for Mg, Acta Mater 56 (2008) 2456e2468.

[50] M.R. Barnett, N. Stanford, A. Ghaderi, F. Siska, Plastic relaxation of the internal stress induced by twinning, Acta Mater 61 (2013) 7859–7867.

[51] M.A. Gharghouri, G.C. Weatherly, J.D. Embury, The interaction of twins and precipitates in a Mg-7.7 at.% Al alloy, Philos. Mag. A 78 (1998) 1137–1149.

[52] K.Y. Xie, D. Zhao, B. Leu, X. Ma, Q. Jiao, J.A. El-Awady, T.P. Weihs, I.J. Beyerlein, M.A. Kumar, Understanding the interaction of extension twinning and basal-plate precipitates in Mg-9Al using precession electron diffraction, Materialia 15 (2021), 101044.

[53] B. Leu, M.A. Kumar, K.Y. Xie, I.J. Beyerlein, Twinning pathways enabled by precipitates in AZ91, Materialia 21 (2022), 101292.